Mode Locking between Helimagnetism and Ferromagnetism

Jingyi Chen,[1,*] Haonan Jin,[1,2,*] Ethan L. Arnold,[3,4] Gerrit van der Laan,[4] Thorsten Hesjedal,[3] and Shilei Zhang[†1,2,5]

[1]*School of Physical Science and Technology, ShanghaiTech University, Shanghai 201210, China*

[2]*ShanghaiTech Laboratory for Topological Physics, ShanghaiTech University, Shanghai 201210, China*

[3]*Department of Physics, Clarendon Laboratory, University of Oxford, Oxford OX1 3PU, United Kingdom*

[4]*Diamond Light Source, Harwell Science and Innovation Campus, Didcot OX11 0DE, United Kingdom*

[5]*Center for Transformative Science, ShanghaiTech University, Shanghai 201210, China*

(Dated: November 23, 2025)

Abstract

Non-collinear spin textures, such as spin spirals and skyrmions, exhibit rich emergent physics in their spin dynamics. Nevertheless, the potential to utilize their distinctive spin resonance characteristics for on-chip microwave magnonic applications is rarely explored. Here, we demonstrate the microwave emission and mode coupling from the resonating spin spiral lattice in a Cu_2OSeO_3/Pt/NiFe heterostructure. We use time-resolved resonant elastic x-ray scattering to visualise the exact vectorial spin precession modes from the two magnetic species in real-time. Our results show that the ferromagnetic NiFe layer dynamically captures the excitation modes of the conical order in helimagnet Cu_2OSeO_3. The off-resonance NiFe spin precession is phase-locked to the helimagnet with a fixed offset, thereby presenting distinct chiral dynamics. This demonstrates that the magnons produced in the process—referred to as helimagnons—can wirelessly transmit spin information at gigahertz frequencies, opening new avenues for on-chip microwave magnonics.

Collective spin excitations in magnetic materials, or magnons, have been extensively utilized in magnonics, significantly advancing information technology and microwave signal processing [1–5]. Recent developments in noncollinear magnetic textures, such as spin helices [6] and skyrmions, have revealed a wealth of intriguing spin dynamics phenomena [7–10], including magnon band folding [11–14], nonreciprocal spin wave transport [15–18], and unique effects like the Archimedean screw and Floquet properties [19]. Despite the promise of these dynamical properties, the applications that harness their nontrivial ferromagnetic resonance features for on-chip magnonic applications remain unexplored.

Helimagnets, such as MnSi [20], FeGe [21], and Cu_2OSeO_3 [22], exhibit a typical noncollinear magnetic phase, where the ground state is characterized by a one-dimensional spin helical cycloid. This state arises from the competition between Heisenberg exchange and Dzyaloshinskii-Moriya interaction [23]. In the presence of a moderate external magnetic field, the spin spiral undergoes incommensurate modulation along the direction of the applied field ($\mathbf{H}_{\mathrm{dc}}$), resulting in a conical phase with a fixed chirality [20]. The excitation spectrum of this conical phase is described by helimagnon theory [10, 24–26], where spin

* These authors contributed equally to this work.

resonance can be induced by an oscillating magnetic field ($\mathbf{H}_{\mathrm{rf}}$), leading to the emergence of two distinct eigenmodes, known as the $-Q$ and $+Q$ modes [7, 9].

Unlike conventional ferromagnetic modes, conical resonance displays unique spin modulation patterns in both space and time. As shown in the blue panels of Fig. 1(a,b), each spin precesses around its local equilibrium position along the one-dimensional, right-handed conical spin chain. Notably, neighbouring spins exhibit a fixed phase delay in time, allowing for the identification of two distinct spin dynamic modes: a positive phase delay along the z-axis for the $+Q$ mode and a negative phase delay for the $-Q$ mode [7, 9, 10]. In this study, we explore the distinctive microwave characteristics generated by these conical modes and investigate how these signals couple to a spatially separated ferromagnet.

An ideal model system to study this phenomenon is illustrated in Fig. 1(a), where ferromagnetic resonance is excited in the conical order in the helimagnet Cu_2OSeO_3 under orthogonal static ($\mathbf{H}_{\mathrm{dc}}$) and oscillating ($\mathbf{H}_{\mathrm{rf}}$) magnetic fields, with an eigenfrequency of ω_{rf}. The resulting temporally modulated spin texture emits a characteristic microwave pattern at ω_{rf} via the oscillating dipolar field, which subsequently couples to a separate soft ferromagnet (a NiFe thin film in this case) positioned at a distance from the helimagnet. Our theoretical calculations indicate that the ac-susceptibility of the NiFe film sharply increases as the conical phase matches resonance, and that the NiFe spin precession becomes phase-locked to the helimagnons with a characteristic offset (see Supplementary Section S1.2 and Fig. S2). In particular, in the $-Q$ excitation state, the NiFe moments collectively precess around a fixed direction, as shown in Fig. 1(a), with the spin oscillation modes of the two species locked at a fixed phase difference, resembling interlocking gears (see Supplementary Movie 1). Conversely, for the $+Q$ mode, the phase lock presents a 180° phase shift compared to the $-Q$ case, as depicted in Fig. 1(b). Additionally, reversing the chirality of the conical spin chain causes the precession axis of the NiFe spins to be pinned in the opposite direction, as shown in Fig. 1(c,d). This demonstrates that the chiral symmetry of the helimagnet is transferred to the ferromagnet in its spin dynamics.

This heterostructure system serves not only as an ideal platform for investigating the mode coupling mechanisms from non-trivial helimagnons but also as a prototype for hybrid magnonic devices that harness the unique spin resonance properties of helimagnetism. Essentially, the conical spin order acts as a resonator that transmits signals, while the soft ferromagnet wirelessly receives the microwave signals. However, conducting such experi-

mental work presents significant challenges, as it requires an advanced time-resolved characterization technique capable of simultaneously and individually measuring the vectorial spin dynamics of both magnetic species.

Our approach utilizes resonant elastic x-ray scattering (REXS) [27, 28], leveraging its exceptional capabilities for fast time resolution [29, 30], element-specific detection [31], and vectorial spin sensitivity [32–36]. As illustrated in Fig. 2(b), the target sample consists of a (001)-oriented Cu_2OSeO_3 substrate and a 46-nm-thick NiFe thin film with easy-plane anisotropy [37], separated by a non-magnetic spacer. To optimize the growth conditions [31, 38, 39], a Pt layer is used to spatially isolate the two magnetic species; a thickness of 6 nm is sufficient to prevent other unwanted physical interactions, such as direct exchange coupling [38], mode hybridization [40], or spin pumping [41, 42]. The latter point is discussed in more detail in Supplementary Section S6 and Fig. S15. Figure 2(a) depicts the experimental setup, where time-resolved REXS is performed using a stroboscopic technique.

For a static magnetic structure, REXS in reflection geometry with a scattering angle of 2α exhibits pronounced magnetic sensitivity with element-specific selectivity [43]. By tuning the photon energy to the Cu L_3 (931.25 eV) and Fe L_3 (707 eV) edges, the magnetic structures $\mathbf{m}^{\mathrm{Cu}}$ and $\mathbf{m}^{\mathrm{Fe}}$ can be distinctly characterized by analysing their respective REXS intensities, I^{Cu} and I^{Fe} [31]. When the system is driven into magnetic resonance, the time-evolving mode can be constructed by capturing a series of static spin textures at each frozen time frame. As shown in Fig. 2(a), our REXS measurements at the synchrotron are performed at a 0.5 GHz repetition frequency (equivalent to 2 ns intervals between successive shots), with each shot having a pulse width of 35 ps. This frequency is synchronized and multiplied with a gigahertz-level microwave signal (i.e., $\omega_{\mathrm{rf}} = 0.5 \times n$ GHz; $n = 1, 2, ...$), which subsequently drives the sample into ferromagnetic resonance through a two-port coplanar waveguide (see Methods for setup details). An arbitrary time delay t between the probing REXS modulation and the pumping microwave can be precisely controlled, allowing the measured instantaneous spin structures from I as a function of t to effectively reconstruct a dynamic movie of a particular resonance mode.

Throughout the experiments, the incident beam is set to be left-circularly polarized. Two detection channels are monitored simultaneously: (i) the microwave transmission power S_{21}, detected at port 2 [see Fig. 2(a)], and (ii) a photodiode that measures the scattering intensity. To improve the spin sensitivity, a phase modulation (PM) lock-in technique is

employed, from which the measured signal I_{PM} equals to the REXS intensity difference from the two time steps that are separated by a phase of 180°, i.e., $I_{\mathrm{PM}}(t) = I(t) - I(t+\tau)$, where $\tau = 1/(2\omega_{\mathrm{rf}})$ is the half periodicity of the spin resonance. This approach effectively suppresses contributions from non-magnetic scattering events (see Supplementary Section S2.2, Eqs. S14–S16), leading to straightforward extraction of the vectorial spin dynamics.

We then establish a direct relation between $I(t)$ and the spin resonance mode. The complete theoretical treatment and numerical simulations are detailed in Methods and Supplementary Sections S2.1 and S2.3. Based on our simulations, the full dynamics of a resonating spin $\mathbf{m}(t)$, in our hybrid system can be parameterized by a four-angle model – $(\Theta, \Psi, \xi, \phi)$. We note that our four-angle model, which can be considered a simplified version of the well-established Smit-Beljers precession model [44] (commonly used for ferromagnetic resonance simulations), is sufficient for our system as discussed in Supplementary Section S8 and Fig. S16. As illustrated in Fig. 2(c), in the absence of the pumping microwave, the magnetic moment remains in its equilibrium position, denoted as $\hat{n}_3$, and is described by the polar and the azimuthal angles (Θ, Ψ). When the microwave is switched on, the spin begins to precess around $\hat{n}_3$ with a precession angle ξ and a dynamic phase ϕ. Thus, the exact mode can be expressed mathematically as:

$$\mathbf{m}(t) = \begin{pmatrix} m_x(t) \\ m_y(t) \\ m_z(t) \end{pmatrix} = \mathcal{R}_\Psi \mathcal{R}_\Theta \begin{pmatrix} \sin\xi\cos(2\pi\omega_{\mathrm{rf}}t + \phi) \\ \sin\xi\sin(2\pi\omega_{\mathrm{rf}}t + \phi) \\ \cos\xi \end{pmatrix} \quad , \tag{1}$$

where $\mathcal{R}_\Theta(\mathcal{R}_\Psi)$ is the 3×3 rotation matrix that performs rotations around the y-axis by an angle Θ and around the z-axis by an angle Ψ, respectively (see Methods).

For NiFe, a uniform spin precession is expected [37], and a standard thin-film reflectivity geometry is employed with varying α. At Fe L_3 edge, the expected instantaneous $I(t)$ profile is written as:

$$I^{\mathrm{Fe}}(t) = \mathcal{Y}\{\cos^2\alpha[m_x^{\mathrm{Fe}}(t)]^2 + \frac{1}{2}\sin^2 2\alpha[m_y^{\mathrm{Fe}}(t)]^2 + \sin^2\alpha[m_z^{\mathrm{Fe}}(t)]^2\} \quad , \tag{2}$$

where $\mathcal{Y}$ is a constant that is both t- and $\mathbf{m}$-independent (see Supplementary Section S2.1 and S2.3).

For Cu_2OSeO_3, Θ^{Cu} is uniform, and Ψ^{Cu} is modulated along the z-axis [9]. For simplicity, we only show the conical spin at the top surface (i.e., $z = z_t$), $\mathbf{m}^{\mathrm{Cu}}(z_t, t)$ in the figures, as

the rest spin states throughout the sample, $\mathbf{m}^{\mathrm{Cu}}(z,t)$, can be subsequently determined for a given $+Q$ or $-Q$ mode [7, 9, 10] (see in Fig. 1). At Cu L_3 edge, the scattering condition is set to $2\alpha \approx 97°$, which coincides with the (001)-Bragg peak. This leads to a similar $I^{\mathrm{Cu}}(t)$ profile with that of in Eq. (2), i.e., $I^{\mathrm{Cu}}(t) = f[m_x^{\mathrm{Cu}}(t), m_y^{\mathrm{Cu}}(t), m_z^{\mathrm{Cu}}(t)]$ (see Supplementary Section S2.1 and Eq. S10).

In summary, for either Cu or Fe spins, a specific four-angle model of $(\Theta, \Psi, \xi, \phi)$ fully defines a precessional mode $\mathbf{m}(t)$, which leads to an $I(t)$ profile. Consequently, the expected dynamical curve of $I_{\mathrm{PM}}(t) = I(t) - I(t+\tau)$ is obtained, which can be quantitatively compared with the measured data. This way, an iterative fitting algorithm can be established, from which a reliable $\mathbf{m}(t)$ movie is constructed.

We first determine the experimental conditions for the two modes using the S_{21} channel. Figure 2(d) presents the magnetic phase diagram of the Cu_2OSeO_3 substrate, showing that the conical phase can be stabilized over a wide range of temperatures (T) and H_{dc} fields. Nevertheless, to excite a specific resonance mode, a precise combination of $(\omega_{\mathrm{rf}}, H_{\mathrm{dc}}, T)$ is required. Due to instrumental limitations, H_{dc} cannot be varied continuously. Therefore, we use T as a variable, while keeping ω_{rf} and H_{dc} fixed.

Figure 2(e) presents two in-situ temperature scans of the S_{21} parameter, following the measurement paths indicated in Fig. 2(d). The observed microwave absorption behavior aligns with previously reported conical ferromagnetic resonance characteristics, allowing for the precise identification of the helimagnon modes [7, 9, 42]. As shown in the figure, we use a combination of parameters (4 GHz, 15 mT, 42 K) to excite the $+Q$ mode; and (2 GHz, 25 mT, 49 K) to drive the $-Q$ mode. The full $\pm Q$ mode resonance behavior is confirmed by the temperature-dependent FMR maps shown in Supplementary Section S3 and Fig. S4.

After achieving the FMR condition, we use the REXS channel to study the time-resolved spin structures. Figure 2(f) shows a typical example of the measured $I_{\mathrm{PM}}(t)$ data, while Fig. 2(g) represents a typical example of the extracted resonance mode model. In the figures, blue is used to denote data from Cu_2OSeO_3 measured at 931.25 eV (Cu L_3 edge), and green indicates data from NiFe measured at 707 eV (Fe L_3 edge). As shown in Fig. 2(f), for the $+Q$ mode, the $I_{\mathrm{PM}}^{\mathrm{Cu}}(t)$ curve exhibits an oscillatory profile with a periodicity of 250 ps, corresponding to the drive frequency of $\omega_{\mathrm{rf}} = 4$ GHz. Notably, the NiFe layer also responds to the resonance signals from the helimagnet, displaying a pronounced $I_{\mathrm{PM}}^{\mathrm{Fe}}(t)$ amplitude with the same modulation frequency. The time-resolved REXS measurements were performed at

different scattering angles 2α. As illustrated in Fig. 2(f), all REXS profiles show an identical modulation phase at all measured angles, confirming that $\mathbf{m}^{\mathrm{Fe}}(t)$ is indeed uniform along the z-axis [30].

TABLE I. Refined spin resonance parameters for the two conical modes.

	$+Q$				$-Q$			
	Θ	Ψ	ξ	ϕ	Θ	Ψ	ξ	ϕ
$\mathbf{m}^{\mathrm{Fe}}(t)$	88°	179°	1.8°	−51°	86°	−32°	1.8°	2°
$\mathbf{m}^{\mathrm{Cu}}(z_t, t)$	85.5°	89°	4°	39°	76.5°	−122°	4°	−88°

Next, we extract the precise spin dynamics by applying the iterative fitting algorithm. The initial model parameters $(\Theta, \Psi, \xi, \phi)^{\mathrm{Cu}}/\mathrm{Pt}/(\Theta, \Psi, \xi, \phi)^{\mathrm{Fe}}$ are derived from micromagnetic simulations. They are subsequently optimized by the refinement iterations. The left part in Table I lists the full set of the refined parameters for the $+Q$ mode, which allows for the reconstruction of a spin resonance movie for the hybrid system, as shown in Fig. 2(g). It is evident that the NiFe spin precession axis is nearly in-plane ($\Theta^{\mathrm{Fe}} = 88°$) and is azimuthally pinned to a fixed relative orientation with respect to Ψ^{Cu}, specifically $\Delta\Psi = 90°$. This behavior is consistent with the anisotropy and XMCD data presented in Supplementary Section S7 and Fig. S15, which confirm the absence of out-of-plane resonance in the NiFe layer. Furthermore, the resonating spins of the helimagnet and the ferromagnet are strongly correlated in their rotational phase, maintaining a constant phase difference $\Delta\phi = -90°$ at all times. In other words, for $+Q$ mode, the NiFe spins are interlocked by the conical spins in a specific configuration.

To confirm that the enhancement of spin dynamics in NiFe originates from the helimagnon excitation, we applied the same time-resolved technique while continuously tuning through the $+Q$ resonance. Figure 3(a,b) show the temperature-dependent $I_{\mathrm{PM}}(t)$ curves for NiFe and Cu_2OSeO_3 respectively, measured at 4 GHz and 15 mT, following the same scanning protocol as in Fig. 2(e). In this way, the correlated spin-dynamics of the two species are distinctly resolved across the helimagnon resonance. Following the established iterative algorithm, the temperature-dependent $\mathbf{m}^{\mathrm{Cu}}(z_t, t)$ and $\mathbf{m}^{\mathrm{Fe}}(t)$ functions can be separately reconstructed. The time-averaged, equilibrium positions of both species are temperature-independent, i.e., $\Theta^{\mathrm{Cu}}_{\mathrm{top}} = 85.5°$, $\Psi^{\mathrm{Cu}}_{\mathrm{top}} = 89°$, $\Theta^{\mathrm{Fe}} = 88°$, $\Psi^{\mathrm{Fe}} = 179°$, $\Delta\Psi = 90°$, which are

consistent with the values in Table I. On the other hand, the dynamical angles ξ and ϕ are strongly temperature-dependent, as shown in Fig. 3(c-g).

First, the $+Q$ resonance condition is consistently identified at 42 K. As shown in Fig. 3(d,f), around this temperature (highlighted by the blue-shaded area), the precessing cone angle ξ^{Cu} exhibits a pronounced peak, and its dynamical phase ϕ^{Cu} undergoes a continuous shift. Meanwhile, as shown in Fig. 3(c), the spin precession amplitude ξ^{Fe} in NiFe closely follows the evolution of ξ^{Cu}, reaching its maxima at the same resonance temperature of 42 K. Moreover, as shown in Fig. 3(e), ϕ^{Fe} exhibits a substantial phase shift when traversing the $+Q$ resonance, suggesting that the spin precessions in NiFe and Cu_2OSeO_3 are interlocked. It is worth noting, however, that the total phase shift of ϕ^{Fe} is smaller than that of ϕ^{Cu}, and a phase jump anomaly occurs at 47 K in ϕ^{Fe}. This indicates that NiFe is driven not only by the unique microwave field that is emitted by the helimagnon, but also by parasitic microwave background from the coplanar waveguide (see Supplementary Section S5.3 and Fig. S11). A detailed analysis of the parasitic CPW contribution to the spin precession amplitude is provided in Supplementary Section S4 and Fig. S5. Nevertheless, at the $+Q$ resonance condition, the helimagnon's signal dominates the spin dynamics of the permalloy, effectively transferring its microwave information onto the ferromagnetic thin film.

Such picture is more clearly visualized in the vectorial spin precession model in Fig. 3(g). Under all conditions — whether on- or off-resonance — the NiFe spins are consistently phase-locked with the conical spins with an offset. This suggests that the ferromagnetic layer is sensitive to the microwave signals emitted from the underlying helimagnet.

Turning to the $-Q$ mode, we excite the system with a 2 GHz microwave, as shown in Fig. 4(a). Both species exhibit pronounced REXS modulations with a periodicity of 500 ps, indicating that both $\mathbf{m}^{\mathrm{Cu}}$ and $\mathbf{m}^{\mathrm{Fe}}$ are precessing in a correlated manner. The refined spin dynamics, listed in Table I, reveals a similar mode-locking mechanism. First, the precession axis of the NiFe spin is pinned to the conical precession axis in the same ways as for the $+Q$ mode; specifically, $\hat{n}_3^{\mathrm{Fe}}$ is nearly in-plane, with $\Delta\Psi = 90°$, as shown in Fig. 4(b). More importantly, the dynamical spin rotation between $\mathbf{m}^{\mathrm{Fe}}(t)$ and $\mathbf{m}^{\mathrm{Cu}}(t)$ has an opposite phase difference of $\Delta\phi = 90°$ compared to the $+Q$ mode. This feature aligns with the theoretical predictions shown in Fig. 1.

In summary, the real-time visualization of resonating spins in our hybrid magnonic system reveals the distinct GHz-level microwave characteristics emitted by an excited helimagnon.

We have demonstrated that such an rf signal can be effectively detected by a remote ferromagnet, whose spins are dynamically coupled to the signal source in a manner resembling an interlocking gear mechanism. This presents a potential wireless communication solution in magnonics based on noncollinear spin dynamics. Moreover, this time-resolved experimental technique can be broadly applied to explore a wide range of spin dynamics phenomena.

Acknowledgements. This work was supported by the National Key R&D Program of China under contract numbers 2022YFA1403602 and 2020YFA0309400, the Science and Technology Commission of the Shanghai Municipality (21JC1405100), the National Natural Science Foundation of China (Grant nos. 12074257 and 12241406), and the Double First-Class Initiative Fund of ShanghaiTech University. Diamond Light Source is acknowledged for beamtime on beamline I10 under proposal MM36751.

Author contributions

S.L.Z. conceived and supervised the project. C.J.Y., H.N.J., G.L., T.H. and S.L.Z. performed the experiments and analysed the data. S.L.Z. wrote the paper with input from all authors. All authors discussed the results and contents of the paper.

Data availability

The data that support the findings of this study are available from the corresponding authors upon reasonable request.

Code availability

The refinement algorithm for obtaining the resonating modes is available from the corresponding authors upon reasonable request.

Author information

School of Physical Science and Technology, ShanghaiTech University, Shanghai 201210, China

Jingyi Chen, Haonan Jin & Shilei Zhang

ShanghaiTech Laboratory for Topological Physics, ShanghaiTech University, Shanghai 201210, China

Haonan Jin & Shilei Zhang

Center for Transformative Science, ShanghaiTech University, Shanghai 201210, China

Shilei Zhang

Magnetic Spectroscopy, Diamond Light Source, Harwell Science and Innovation Campus, Didcot OX11 0DE, United Kingdom

Gerrit van der Laan

Department of Physics, Clarendon Laboratory, University of Oxford, Oxford OX1 3PU, United Kingdom

Thorsten Hesjedal

Corresponding author

Correspondence to Shilei Zhang

Ethics declarations

Competing interests

The authors declare no competing interests.

Supplementary information

Supplementary Sections S1-S8 and Figs. S1-S17.

Supplementary Movie 1: Dynamical mode communication between the resonating conical spins and the pick-up NiFe spins.

References

[1] A. A. Serga, A. V. Chumak, and B. Hillebrands, YIG magnonics, J. Phys. D: Appl. Phys. **43**, 264002 (2010).

[2] A. V. Chumak, V. I. Vasyuchka, A. A. Serga, and B. Hillebrands, Magnon spintronics, Nat. Phys. **11**, 453 (2015).

[3] P. Pirro, V. I. Vasyuchka, A. A. Serga, and B. Hillebrands, Advances in coherent magnonics, Nat. Rev. Mater. **6**, 1114 (2021).

[4] B. Flebus, D. Grundler, B. Rana, Y. Otani, I. Barsukov, A. Barman, G. Gubbiotti, P. Landeros, J. Akerman, U. Ebels, P. Pirro, V. E. Demidov, K. Schultheiss, G. Csaba, Q. Wang, F. Ciubotaru, D. E. Nikonov, P. Che, R. Hertel, T. Ono, D. Afanasiev, J. Mentink, T. Rasing, B. Hillebrands, S. V. Kusminskiy, W. Zhang, C. R. Du, A. Finco, T. van der Sar, Y. K. Luo, Y. Shiota, J. Sklenar, T. Yu, and J. Rao, The 2024 magnonics roadmap, J. Phys.: Cond. Matter **36**, 363501 (2024).

[5] Q. Wang, G. Csaba, R. Verba, A. V. Chumak, and P. Pirro, Nanoscale magnonic networks, Phys. Rev. Appl. **21**, 040503 (2024).

[6] M. Uchida, Y. Onose, Y. Matsui, and Y. Tokura, Real-space observation of helical spin order, Science **311**, 359 (2006).

[7] Y. Onose, Y. Okamura, S. Seki, S. Ishiwata, and Y. Tokura, Observation of magnetic excitations of skyrmion crystal in a helimagnetic insulator Cu_2OSeO_3, Phys. Rev. Lett. **109**, 037603 (2012).

[8] J. D. Koralek, D. Meier, J. P. Hinton, A. Bauer, S. A. Parameswaran, A. Vishwanath, R. Ramesh, R. W. Schoenlein, C. Pfleiderer, and J. Orenstein, Observation of coherent helimagnons and Gilbert damping in an itinerant magnet, Phys. Rev. Lett. **109**, 247204 (2012).

[9] T. Schwarze, J. Waizner, M. Garst, A. Bauer, I. Stasinopoulos, H. Berger, C. Pfleiderer, and D. Grundler, Universal helimagnon and skyrmion excitations in metallic, semiconducting and insulating chiral magnets, Nat. Mater. **14**, 478 (2015).

[10] M. Garst, J. Waizner, and D. Grundler, Collective spin excitations of helices and magnetic skyrmions: Review and perspectives of magnonics in non-centrosymmetric magnets, J. Phys.

D: Appl. Phys. **50**, 293002 (2017).

[11] M. Kugler, G. Brandl, J. Waizner, M. Janoschek, R. Georgii, A. Bauer, K. Seemann, A. Rosch, C. Pfleiderer, P. Böni, and M. Garst, Band structure of helimagnons in MnSi resolved by inelastic neutron scattering, Phys. Rev. Lett. **115**, 097203 (2015).

[12] M. Weiler, A. Aqeel, M. Mostovoy, A. Leonov, S. Geprägs, R. Gross, H. Huebl, T. T. Palstra, and S. T. Goennenwein, Helimagnon resonances in an intrinsic chiral magnonic crystal, Phys. Rev. Lett. **119**, 237204 (2017).

[13] T. Weber, D. M. Fobes, J. Waizner, P. Steffens, G. S. Tucker, M. Böhm, L. Beddrich, C. Franz, H. Gabold, R. Bewley, D. Voneshen, M. Skoulatos, R. Georgii, G. Ehlers, A. Bauer, C. Pfleiderer, P. Böni, M. Janoschek, and M. Garst, Topological magnon band structure of emergent Landau levels in a skyrmion lattice, Science **375**, 1025 (2022).

[14] Y. Shimamoto, Y. Matsushima, T. Hasegawa, Y. Kousaka, I. Proskurin, J. Kishine, A. Ovchinnikov, F. Goncalves, and Y. Togawa, Observation of collective resonance modes in a chiral spin soliton lattice with tunable magnon dispersion, Phys. Rev. Lett. **128**, 247203 (2022).

[15] Y. Okamura, F. Kagawa, M. Mochizuki, M. Kubota, S. Seki, S. Ishiwata, M. Kawasaki, Y. Onose, and Y. Tokura, Microwave magnetoelectric effect via skyrmion resonance modes in a helimagnetic multiferroic, Nat. Commun. **4**, 2391 (2013).

[16] T. Nomura, X.-X. Zhang, S. Zherlitsyn, J. Wosnitza, Y. Tokura, N. Nagaosa, and S. Seki, Phonon magnetochiral effect, Phys. Rev. Lett. **122**, 145901 (2019).

[17] N. Ogawa, L. Köhler, M. Garst, S. Toyoda, S. Seki, and Y. Tokura, Nonreciprocity of spin waves in the conical helix state, Proc. Natl. Acad. Sci. U.S.A. **118**, e2022927118 (2021).

[18] T. Nomura, X.-X. Zhang, R. Takagi, K. Karube, A. Kikkawa, Y. Taguchi, Y. Tokura, S. Zherlitsyn, Y. Kohama, and S. Seki, Nonreciprocal phonon propagation in a metallic chiral magnet, Phys. Rev. Lett. **130**, 176301 (2023).

[19] N. del Ser, L. Heinen, and A. Rosch, Archimedean screw in driven chiral magnets, SciPost Phys. **11**, 009 (2021).

[20] S. Mühlbauer, B. Binz, F. Jonietz, C. Pfleiderer, A. Rosch, A. Neubauer, R. Georgii, and P. Böni, Skyrmion lattice in a chiral magnet, Science **323**, 915 (2009).

[21] X. Z. Yu, N. Kanazawa, Y. Onose, K. Kimoto, W. Z. Zhang, S. Ishiwata, Y. Matsui, and Y. Tokura, Near room-temperature formation of a skyrmion crystal in thin-films of the helimagnet FeGe, Nat. Mater. **10**, 106 (2011).

[22] S. Seki, X. Z. Yu, S. Ishiwata, and Y. Tokura, Observation of skyrmions in a multiferroic material, Science **336**, 198 (2012).

[23] N. Nagaosa and Y. Tokura, Topological properties and dynamics of magnetic skyrmions, Nat. Nanotech. **8**, 899 (2013).

[24] M. Date, K. Okuda, and K. Kadowaki, Electron spin resonance in the itinerant-electron helical magnet MnSi, J. Phys. Soc. Jpn. **42**, 1555 (1977).

[25] M. Kataoka, Spin waves in systems with long period helical spin density waves due to the antisymmetric and symmetric exchange interactions, J. Phys. Soc. Jpn. **56**, 3635 (1987).

[26] D. Belitz, T. R. Kirkpatrick, and A. Rosch, Theory of helimagnons in itinerant quantum systems, Phys. Rev. B **73**, 054431 (2006).

[27] J. P. Hannon, G. T. Trammell, M. Blume, and D. Gibbs, X-ray resonance exchange scattering, Phys. Rev. Lett. **61**, 1245 (1988).

[28] G. van der Laan, Soft x-ray resonant magnetic scattering of magnetic nanostructures, C. R. Physique **9**, 570 (2008).

[29] D. M. Burn, S. Zhang, K. Zhai, Y. Chai, Y. Sun, G. van der Laan, and T. Hesjedal, Mode-resolved detection of magnetization dynamics using x-ray diffractive ferromagnetic resonance, Nano Lett. **20**, 345 (2019).

[30] D. M. Burn, S. L. Zhang, G. Q. Yu, Y. Guang, H. J. Chen, X. P. Qiu, G. van der Laan, and T. Hesjedal, Depth-resolved magnetization dynamics revealed by x-ray reflectometry ferromagnetic resonance, Phys. Rev. Lett. **125**, 137201 (2020).

[31] K. Ran, Y. Liu, H. Jin, Y. Shangguan, Y. Guang, J. Wen, G. Yu, G. van der Laan, T. Hesjedal, and S. Zhang, Axially bound magnetic skyrmions: Glueing topological strings across an interface, Nano Lett. **22**, 3737 (2022).

[32] M. Blume and D. Gibbs, Polarization dependence of magnetic x-ray scattering, Phys. Rev. B **37**, 1779 (1988).

[33] D. Gibbs, D. R. Harshman, E. D. Isaacs, D. B. McWhan, D. Mills, and C. Vettier, Polarization and resonant properties of magnetic x-ray scattering in holmium, Phys. Rev. Lett. **61**, 1241 (1988).

[34] S. L. Zhang, G. van der Laan, and T. Hesjedal, Direct experimental determination of spiral spin structures via the dichroism extinction effect in resonant elastic soft x-ray scattering, Phys. Rev. B **96**, 094401 (2017).

[35] S. L. Zhang, G. van der Laan, and T. Hesjedal, Direct experimental determination of the topological winding number of skyrmions in Cu_2OSeO_3, Nat. Commun. **8**, 14619 (2017).

[36] S. Zhang, G. van der Laan, W. Wang, A. Haghighirad, and T. Hesjedal, Direct observation of twisted surface skyrmions in bulk crystals, Phys. Rev. Lett. **120**, 227202 (2018).

[37] E. F. Silva, M. A. Corrêa, R. D. Della Pace, C. C. Plá Cid, P. R. Kern, M. Carara, C. Chesman, O. A. Santos, R. L. Rodríguez-Suárez, A. Azevedo, S. M. Rezende, and F. Bohn, Thickness dependence of the magnetic anisotropy and dynamic magnetic response of ferromagnetic NiFe films, J. Phys. D: Appl. Phys. **50**, 185001 (2017).

[38] K. Ran, Y. Liu, Y. Guang, D. M. Burn, G. van der Laan, T. Hesjedal, H. Du, G. Yu, and S. Zhang, Creation of a chiral bobber lattice in helimagnet-multilayer heterostructures, Phys. Rev. Lett. **126**, 017204 (2021).

[39] H. Jin, W. Tan, Y. Liu, K. Ran, R. Fan, Y. Shangguan, Y. Guang, G. van der Laan, T. Hesjedal, J. Wen, G. Yu, and S. Zhang, Evolution of emergent monopoles into magnetic skyrmion strings, Nano Lett. **23**, 5164 (2023).

[40] C. Lüthi, L. Flacke, A. Aqeel, A. Kamra, R. Gross, C. Back, and M. Weiler, Hybrid magnetization dynamics in Cu_2OSeO_3/NiFe heterostructures, Appl. Phys. Lett. **122**, 012401 (2023).

[41] D. Hirobe, Y. Shiomi, Y. Shimada, J. ichiro Ohe, and E. Saitoh, Generation of spin currents in the skyrmion phase of a helimagnetic insulator Cu_2OSeO_3, J. Appl. Phys. **117**, 053904 (2015).

[42] W. Tan, H. Jin, R. Fan, K. Ran, and S. Zhang, Evidence for giant surface Dzyaloshinskii-Moriya interaction in the chiral magnetic insulator Cu_2OSeO_3, Phys. Rev. B **109**, L220402 (2024).

[43] S. L. Zhang, A. Bauer, H. Berger, C. Pfleiderer, G. van der Laan, and T. Hesjedal, Resonant elastic x-ray scattering from the skyrmion lattice in Cu_2OSeO_3, Phys. Rev. B **93**, 214420 (2016).

[44] J. Smit and H. G. Beljers, Ferromagnetic resonance absorption in $BaFe_{12}O_{10}$, Philips Res. Rep. **10**, 113 (1955)

METHODS

Sample preparation

Single-crystalline Cu_2OSeO_3 was grown by chemical vapour transport, and its high crystalline quality was confirmed by x-ray diffraction. The (001) surface was subsequently polished until the roughness reaches wafer-quality. The total thickness of the crystal measures $100\,\mu$m, which enables full penetration of the in-plane microwave field component through the sample. Next, Pt(6 nm)/NiFe(46 nm) was grown on top of the Cu_2OSeO_3 substrate using standard DC magnetron sputtering technique. The film thickness, as well as the sharp interfaces were confirmed by soft x-ray reflectivity during the beamtime.

Time-resolved REXS measurements

Element- and time-resolved spin dynamics were measured using stroboscopic resonant elastic x-ray scattering (REXS) on beamline I10 at Diamond Light Source. The sample was mounted in reflection geometry with the scattering angle set to $2\alpha = 97^\circ$ at the Cu L_3 edge (931.25 eV) and $2\alpha = 8^\circ$ at the Fe L_3 edge (707 eV). The incident beam was left-circularly polarized throughout all measurements.

A microwave excitation was applied via a two-port coplanar waveguide, which generated an out-of-plane oscillating magnetic field $H_{\mathrm{rf}}(t) = H_0 \sin(\omega_{\mathrm{rf}} t)$ with $H_0 \approx 0.1\,\mathrm{mT}$. The microwave frequency was set by multiplying a 0.5 GHz clock signal by an integer n, yielding $\omega_{\mathrm{rf}} = n \times 0.5\,\mathrm{GHz}$. The sample was driven into ferromagnetic resonance by matching this excitation to the eigenmodes of the underlying conical magnetic order.

The synchronization between x-ray probing and microwave driving was achieved via phase modulation. The 0.5 GHz clock signal was passed through a phase modulator that toggled the phase by 180° every 0.808 ms (1.237 kHz). The probe–pump delay was adjusted using a high-precision delay line with picosecond resolution, enabling fine sampling of the spin precession over the 2 ns stroboscopic window defined by the 0.5 GHz storage-ring repetition rate. The REXS signal was recorded by a photodiode synchronized to the modulation frequency, enabling lock-in detection of the phase-modulated signal.

This technique yields the differential intensity

$$I_{\mathrm{PM}}(t) = I(t) - I(t+\tau), \tag{3}$$

where $\tau = 1/(2\omega_{\mathrm{rf}})$. This suppresses static or non-magnetic background, isolating the contribution from coherent spin precession.

Micromagnetic simulations

Micromagnetic simulations were carried out using the Mumax3 package to model the Cu_2OSeO_3/Pt/NiFe heterostructure. The system was discretized on a three-dimensional finite-difference grid with a cell size of $2 \times 2 \times 2\,\mathrm{nm}^3$. Periodic boundary conditions were imposed in the in-plane (x and y) directions, while an open boundary condition was used along z. Non-local dipolar interactions were included in all simulations.

The simulated heterostructure consisted of a 46 nm-thick NiFe layer, a 6 nm Pt spacer layer, and a 2248 nm-thick Cu_2OSeO_3 substrate, with lateral dimensions $40 \times 40\,\mathrm{nm}^2$ for all layers. For NiFe, a saturation magnetization of 8.6×10^5 A/m, an exchange stiffness of 1.3×10^{-11} J/m, and a Gilbert damping constant of 0.008 were used; the Dzyaloshinskii–Moriya interaction (DMI) was set to zero. For the Cu_2OSeO_3 layer, the saturation magnetization was 1.044×10^5 A/m, the exchange stiffness was 3.547×10^{-13} J/m, and the bulk DMI constant was $7.43 \times 10^{-5}\,\mathrm{J/m}^2$, with a damping constant of 0.01. The Pt spacer was modelled as a non-magnetic layer with vanishing magnetic parameters.

To obtain the equilibrium magnetic textures of the helimagnet, the system was relaxed under a static field $H_{\mathrm{dc}} \parallel z$, reproducing the helical, conical, and field-polarized phases of Cu_2OSeO_3. The dynamical response was then computed by applying a sinusoidal excitation field

$$H_{\mathrm{rf}}(t) = H_0 \sin(\omega_{\mathrm{rf}} t),$$

with $H_0 = 0.1\,\mathrm{mT}$ along the x-direction, and integrating the Landau–Lifshitz–Gilbert equation for 30 ns under both H_{dc} and H_{rf}. From the time-dependent magnetization $m(z,t)$, the ac-susceptibility spectra $\chi_{\mathrm{Cu}}(\omega_{\mathrm{rf}})$ and $\chi_{\mathrm{Fe}}(\omega_{\mathrm{rf}})$ were extracted by sweeping the drive frequency to identify the $\pm Q$ resonance modes.

Beyond the spectral information, the simulations also provide the full spatiotemporal precession patterns of the conical $\pm Q$ modes, including the characteristic phase sequence of

Cu_2OSeO_3 along the z-axis and their phase-locked coupling to the NiFe precession. These simulated precession trajectories serve as the initial models for the subsequent four-angle mode refinement described in the next section.

A complete description of additional simulation procedures is provided in Supplementary Sections S1.1–S1.2.

Theoretical modelling and mode reconstruction

The spin precession dynamics in both Cu_2OSeO_3 and NiFe are described using a four-angle model parameterized by $(\Theta, \Psi, \xi, \phi)$, where Θ and Ψ define the static orientation of the local magnetic moment, and ξ and ϕ denote the precession cone angle and dynamic phase, respectively. This formulation provides a practical simplification of the Smit-Beljers formalism by assuming circular spin precession (ellipticity $\beta = 1$), which is justified for conical spin textures and supported by micromagnetic simulations.

The time-dependent magnetic moment $\mathbf{m}(t)$ is given by

$$\mathbf{m}(t) = \begin{pmatrix} m_x(t) \\ m_y(t) \\ m_z(t) \end{pmatrix} = R_\Psi R_\Theta \begin{pmatrix} \sin\xi\cos(2\pi\omega_{\mathrm{rf}}t + \phi) \\ \sin\xi\sin(2\pi\omega_{\mathrm{rf}}t + \phi) \\ \cos\xi \end{pmatrix}, \tag{4}$$

where R_Θ and R_Ψ are rotation matrices that align the local equilibrium moment $\hat{n}_3$ with the laboratory frame, as

$$\mathcal{R}_\Theta = \begin{pmatrix} \cos\Theta & 0 & \sin\Theta \\ 0 & 1 & 0 \\ -\sin\Theta & 0 & \cos\Theta \end{pmatrix} \quad \textbf{and} \quad \mathcal{R}_\Psi = \begin{pmatrix} \cos\Theta & -\sin\Theta & 0 \\ \sin\Theta & \cos\Theta & 0 \\ 0 & 0 & 1 \end{pmatrix} . \tag{5}$$

To relate the spin precession to the measured signal, we model the REXS intensity using magnetic crystalline truncation rod theory. The structure factor $F(q_z, t)$ incorporates both charge and magnetic scattering:

$$F(q_z, t) = \sum_z \frac{1}{\Lambda} e^{-2z\sec\alpha/\Lambda} e^{2\pi i q_z z} \left[f_0 \rho(z) \hat{\epsilon}_s^* \cdot \hat{\epsilon}_i - i f_1 (\hat{\epsilon}_s^* \times \hat{\epsilon}_i) \cdot \mathbf{m}(z, t) \right], \tag{6}$$

where Λ is the penetration depth, f_0 and f_1 are scattering factors, and $\hat{\epsilon}_{i,s}$ are polarization vectors.

The REXS intensity is computed as $I(q_z, t) = |F(q_z, t)|^2$, which separates into charge, magnetic, and interference terms. The lock-in detected signal is obtained via a phase modulation (PM) technique,

$$I_{\mathrm{PM}}(t) = I(t) - I(t + \tau), \tag{7}$$

where $\tau = 1/(2\omega_{\mathrm{rf}})$ corresponds to a 180° phase shift. This method effectively suppresses non-magnetic background and isolates magnetic contributions.

To extract the spin dynamics, we fit the experimental $I_{\mathrm{PM}}(t)$ using an iterative refinement algorithm. The fitting minimizes the chi-squared error between measured and calculated signals, adjusting the four-angle model parameters at each step. Initial guesses for $(\Theta, \Psi, \xi, \phi)$ are obtained from micromagnetic simulations. The process converges to an optimized precession profile $\mathbf{m}(t)$ for each species.

Further calculation details are provided in the Supplementary Sections S2.1–S2.2.

Figures

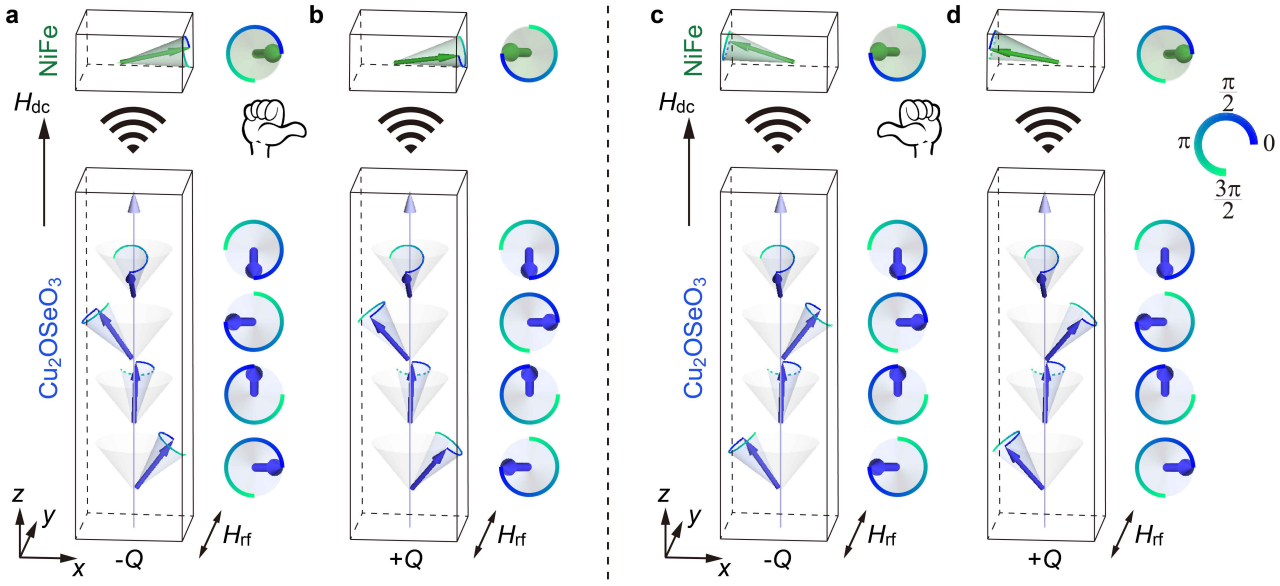

FIG. 1. **Schematic of mode coupling between helimagnet and ferromagnet.** Schematic representation of mode communication between Cu_2OSeO_3 (in blue below) and NiFe (in green above), based on micromagnetic simulations. Panels **a** and **b** depict the excitation of Cu_2OSeO_3 in the $-Q$ and $+Q$ resonance modes for the right-handed conical spiral, while **c** and **d** show the left-handed case. All spins are visualized from two complementary perspectives. The emitted microwaves transmit these modes to the NiFe layer, interlocking its spins to precess in particular ways. As indicated in the legend, the coloured rings represent the spin precession phase, while the arrows denote the zero-phase reference point.

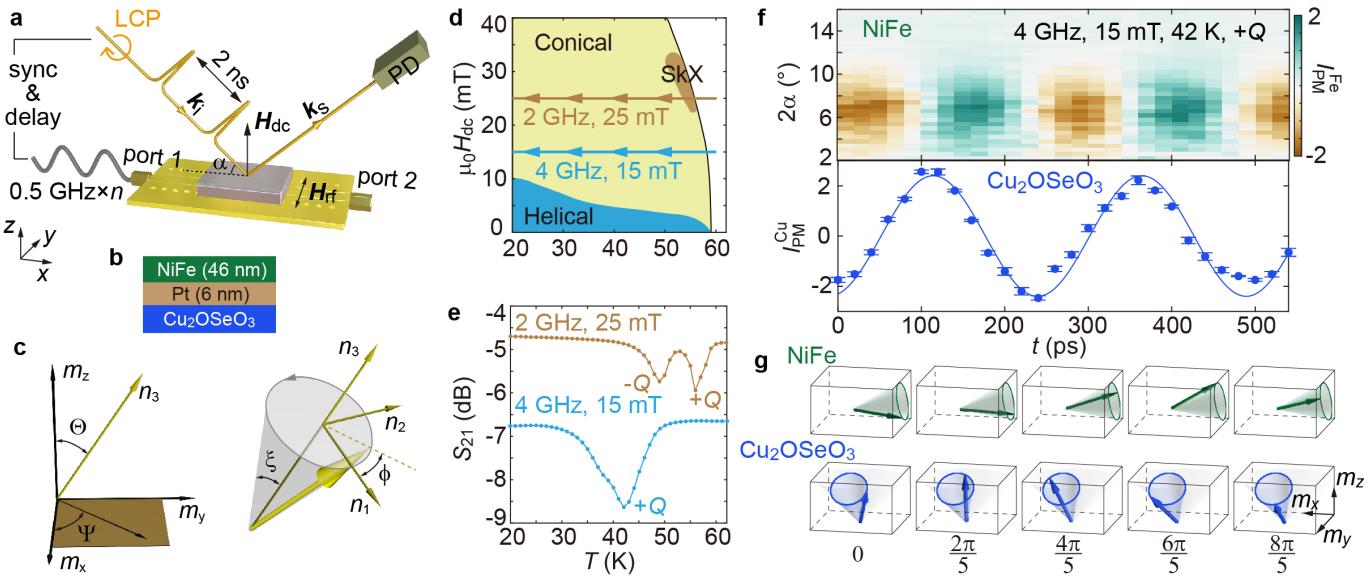

FIG. 2. **Experimental setup and time-resolved Measurement of the $+Q$ mode.** **a**, Schematic of the experimental setup for the time-resolved REXS measurements. **b**, Structural diagram of the Cu_2OSeO_3/Pt/NiFe sample. **c**, The four-angle model that parameterizes the spin resonance mode. Without the pumping microwave, the local spin remains at its equilibrium position along $\mathbf{n}_3$ (left panel), which is described by the polar and azimuthal angles (Θ, Ψ). Upon switching on the microwave (right panel), the spin precesses around $\mathbf{n}_3$ with a cone angle of ξ and a phase of ϕ. **d**, Magnetic phase diagram of Cu_2OSeO_3. The marked paths indicate the two scanning routes for the temperature variation. **e**, S_{21} parameter as a function of temperature, with the brown and blue curves corresponding to the scanning paths in **d**. **f**, Time- and element-resolved REXS data for the $+Q$ mode; blue dots represent the measured data with error bars, and the blue solid line is the fitted curve using the refined model in Table I. **g**, Visualization of the reconstructed $+Q$ mode based on parameters from Table I, with amplified values for Θ^{Cu}, ξ^{Cu}, and ξ^{Fe} for clarity. The five representative time steps over one oscillation period are labeled and displayed. For simplicity, only the top layer spin from the Cu_2OSeO_3 is shown.

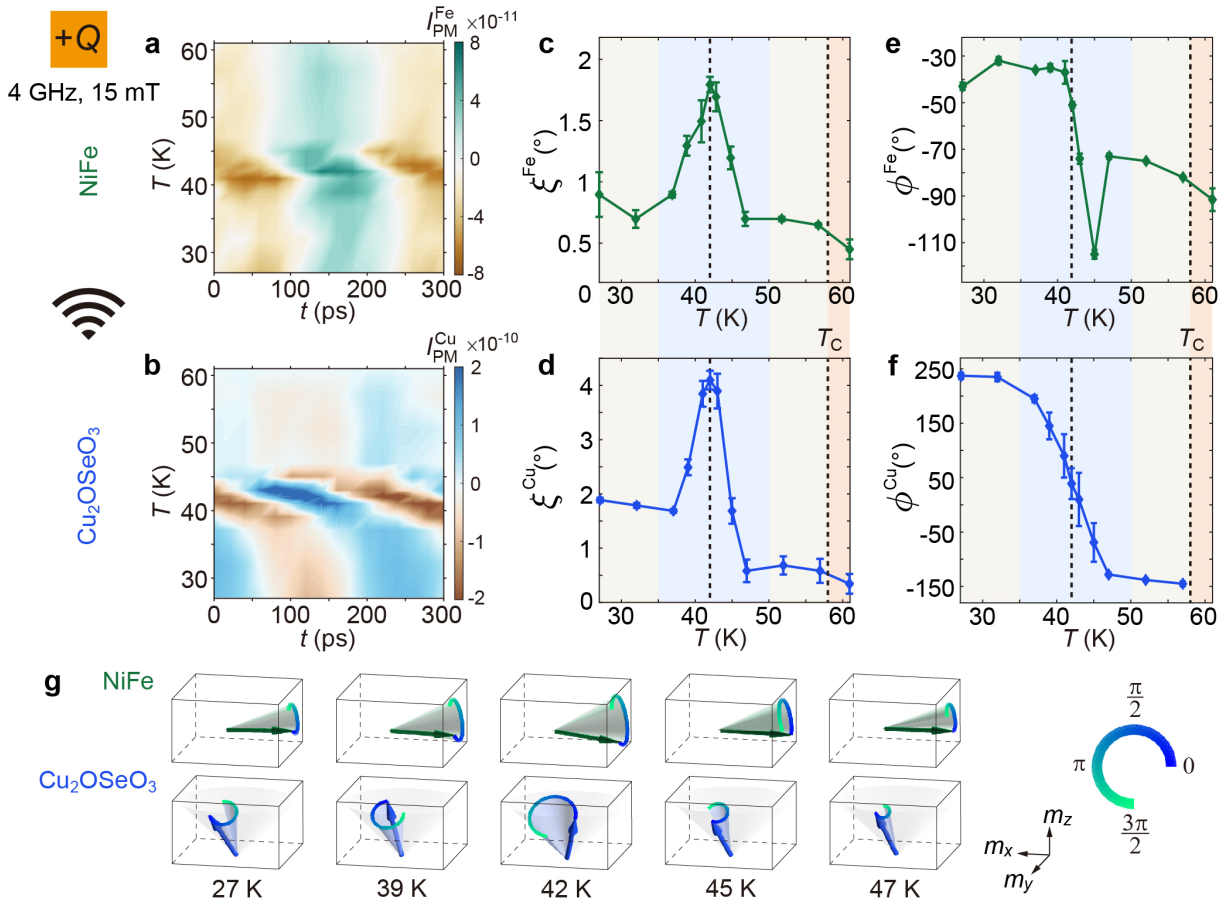

FIG. 3. **Temperature-dependent spin dynamics across the $+Q$ resonance.** Time-resolved REXS profiles measured at various temperatures across the $+Q$ mode for **a**, NiFe and **b**, Cu_2OSeO_3, respectively. Based on **a,b**, the reconstructed precession amplitude ξ as a function of temperature for NiFe and Cu_2OSeO_3 are shown in **c,d** respectively, and their dynamical phase ϕ evolutions are shown in **e,f**. Note that the equilibrium positions of $(\Theta^{\mathrm{Fe}} = 88°, \Psi^{\mathrm{Fe}} = 179°)$ and $(\Theta^{\mathrm{Cu}} = 85.5°, \Psi^{\mathrm{Cu}} = 89°)$ are temperature-independent. The dashed line at 42 K marks the resonance temperature, and the dashed line at 58 K indicates the T_c. The blue-shaded region highlights the on-resonance regime where both ξ and ϕ undergo significant change. **g**, Visualization of the phase-locked spin dynamics at various temperatures. The models are equivalent vectorial representations of **c-f**. Note that the precession angle is amplified for visual clarity. As shown by the legend, the coloured rings indicate the dynamical phase information, where the arrow marks the zero phase. For simplicity, only the top layer spin from the Cu_2OSeO_3 is shown.

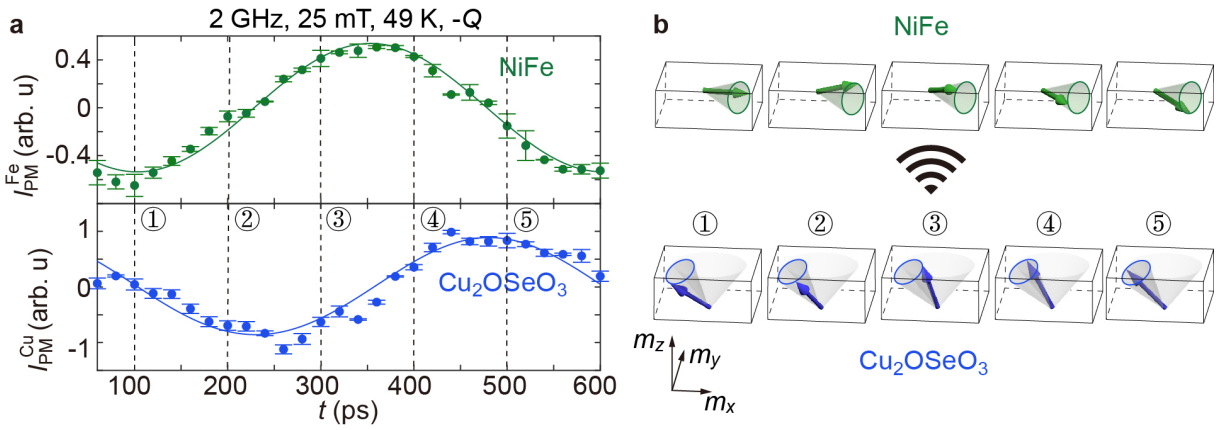

FIG. 4. **Spin dynamics and phase locking for the $-Q$ mode. a**, Time-resolved REXS results for the $-Q$ mode. The dots represent the experimental data, while the solid lines are fitted curves based on the refined mode parameters listed in Table I. **b**, Visualization of the corresponding spin dynamics with the refined parameters from Table I. For enhanced clarity, the values of Θ^{Cu}, ξ^{Cu}, and ξ^{Fe} have been exaggerated, and only the top layer spin from the Cu_2OSeO_3 is shown.